Electronic Supplementary Material (ESI) for Energy & Environmental Science.

This journal is © The Royal Society of Chemistry 2022

## Supplementary Information

**Vacancy rich Al doped MnO$_2$ Cathode breaks the trade-off between kinetics and stability for High-performance Aqueous Zn-ion battery**

Yajun Zhao,[a,b] Shuoxiao Zhang,[c] Yangyang Zhang,[a] Jinrui Liang,[a] Longtao Ren,[a] Hong Jin Fan,*[b] Wen Liu,*[a] Xiaoming Sun*[a]


[a.] Key Laboratory of Chemical Resource Engineering, College of Chemistry, Beijing Advanced Innovation Center for Soft Matter Science and Engineering, Beijing University of Chemical Technology, Beijing, 100029, P. R. China.
[b.] School of Physical and Mathematical Sciences, Nanyang Technological University, Singapore 637371, Singapore
[c.] Department of Physics, City University of Hong Kong, Hong Kong 999077, China.
*Corresponding author. E-mail: fanhj@ntu.edu.sg, wenliu@mail.buct.edu.cn, sunxm@mail.buct.edu.cn

## Experimental Section

### 1. Materials and Methods

#### 1.1 Material and Reagents

$Mn(NO_3)_3 \cdot 6H_2O$, $Al(NO_3)_2 \cdot 9H_2O$, $MnSO_4 \cdot H_2O$, $ZnSO_4 \cdot 7H_2O$ and KOH were purchased from Sigma-Aldrich Co. Ltd and used without further purification. Deionized water (DI water) was used in all the experimental processes.

#### 1.2 Synthesis of $Mn_xAl$-LDHs ($x$=2, 3, 4) and $Mn(OH)_2$ samples

The MnAl-LDH samples were synthesized by a facile electrodeposition method as follows. Carbon cloth (CC) with an area of $3 \times 3$ cm$^2$ was firstly treated by concentrated nitric acid to form hydrophilic surface. Then, $Mn(NO_3)_2 \cdot 6H_2O$ and $Al(NO_3)_3 \cdot 9H_2O$ were mixed in 50 mL DI water with a total metal cation concentration of 1 mM (ratios of Mn and Al were 2:1, 3:1 ,and 4:1) as electrolyte for electrodeposition of $Mn_xAl_1$-LDHs. The CC, saturated calomel electrode, and Pt plate (width: 3 cm, length: 3 cm) were used as working electrode and reference electrode and counter electrode. The electrodeposition process was applied at a voltage of -1.5 V for 600s to obtain $Mn_xAl_1$-LDH on CC. The as-obtained $Mn_3Al_1$-LDHs was rinsed with DI water and dried at 60°C for 2h. The $Mn(OH)_2$ sample was synthesized by a similar electrodeposition procedure for $Mn_xAl_1$-LDHs, but without adding $Al(NO_3)_3 \cdot 9H_2O$.

#### 1.3 Process of electrochemical oxidation for $Al_x$-$MnO_2$ ($x$= 0.05, 0,1, 0.3) and $MnO_2$

The process was carried out by using a cyclic voltammetry (CV) method at a scan rate of 20 mV s$^{-1}$ with operation potential windows within 0-0.6 V vs. SCE in 1 M KOH solution for 30 cycles by using a CorrTest CS2350H electrochemical workstation (Wuhan CorrTest Instrument Corp., Ltd. China) with a three-electrode electrochemical cell at 25 °C, in which the $Mn_xAl_1$-LDHs ($x$= 2, 3, 4) sample was used as work electrode, saturated calomel electrode (SCE) and Pt electrode (width: 3 cm, length: 3 cm) were used as reference and counter electrode, respectively. The $MnO_2$ electrode was synthesized by a similar electrochemical oxidation treatment for $Mn(OH)_2$.

#### 1.4 Electrochemical evaluation

In electrochemical experiment, the Al-$MnO_2$ electrode was *in-situ* grown on CC, and the mass of active materials was about ~1.5 mg. The anode material was used commercial zinc foils. The electrolyte was 2 M $ZnSO_4$ and 0.1 M $MnSO_4$ aqueous electrolyte. Two electrodes were separated by a glass fiber separator. Battery performance tests and Galvanostatic Intermittent Titration Technique (GITT) were conducted with LAND battery testing systems (Wuhan battery technology Co. Ltd, China) and other electrochemical performances such as Cyclic Voltammetry (CV), Electrochemical Impedance Spectroscopy (EIS), were measured on a CHI660E electrochemical workstation.

## 1.5 Material Characterization

XRD patterns were collected using a Bruker DAVINCI D8 ADVANCE diffractometer with Cu Kα radiation (λ = 0.15418 nm) at 40 kV, 30 mA. FT-IR spectra were recorded using a Perkin Elmer GX spectrophotometer. The morphology of the samples was observed by a scanning electron microscope (SEM, Zeiss Supra55) with an accelerating voltage of 20 KV, equipped with an energy dispersive spectroscopy (EDS) to determine the elemental distributions. High-resolution transmission electron microscopy (HRTEM) images were collected by a TECNAI G2 F30 instrument. X-ray photoelectron spectroscopy (XPS, Thermo Electron Corporation ESCALAB 250 XPS spectrometer) were recorded using a twin anode Al Kα X-ray source with a 30 eV pass energy and a 0.5 eV step size. HADDF-STEM observation and EDS mapping was carried out on a JEOL ARM200F (JEOL, Tokyo, Japan) operated at 200 kV with cold filed-emission gun and double hexapole Cs correctors (CEOS GmbH, Heidelberg, Germany). The high resolution powder X-ray diffraction (XRD) experiments were carried out at the PD beamline of the Australia Synchrotron (0.5 mm capillary with a psd photon countering detector and the wavelength was calibrated with a NIST LaB6 660b standard to be 0.6886 Å). Nitrogen adsorption/desorption isotherms were measured using an ASAP 2460 analyzer (Micromeritics, US).

## 2 Theoretical Calculations

Density functional theory (DFT) calculations were performed using the Vienna Ab-initio Simulation Package (VASP) with a supercell of 3×3×1.[1-3] The gradient-corrected exchange correlation functional of Perdew-Burke-Ernzerh generalized-gradient-approximation (PBE-GGA) was employed. A plane-wave basis with 480 eV energy cut-off was adopted using the projector augmented wave (PAW) basis-set and the converge criteria of the force on each relaxed atom below 0.01 eV/Å were used. The convergence criteria were chosen such that the

changes were $10^{-5}$ eV for the energy. A climbing image-nudged elastic band (CI-NEB) method was used to study the diffusion state using $2\times2\times2$ k-point sampling.[4] The calculation of the diffusion barrier of Zn was performed on two models of $Al_{0.1}$-$MnO_2$ and $MnO_2$.

**Supplementary Notes 1: Estimation of the capacitive and diffusion-controlled contributions.**

To analysis the electrode kinetics for Zn storage, the cyclic voltammetry curves at different sweep rates were measured. Generally, the measured peak current ($i$) and sweep rate ($v$) in a CV scan obey a power-law relationship:

$$i = av^b \tag{1}$$

$$\log(i) = \log(a) + b \cdot \log(v) \tag{2}$$

where, $a$ and $b$ are adjustable, and the b value can be attained by fitting slope of the $\log(i)$ versus $\log(v)$ profile. A $b$ value of 1.0 indicates a capacitive dominated charge storage behavior while a $b$ value of 0.5 refers to ionic diffusion-controlled behavior. Furthermore, for a quantitative analysis of diffusion-controlled and capacitive contributions in current response, assumption of an integration of semi-infinite diffusion and capacitive like process were carried out by the following equation:

$$i = k_1v + k_2v^{1/2} \tag{3}$$

The diffusion-controlled and capacitive contributions can be estimated by determining $k_1$ and $k_2$.[5]

**Supplementary Notes 2: Relationship between reversible structural changes and kinetic properties.**

The relationship between the structural variation and corresponding cathode kinetic properties of the diffusion coefficient of zinc ions ($D_{Zn}^{2+}$) were demonstrated by galvanostatic intermittent titration technique (GITT) measurements and were used to calculate based on the following equation:

$$D_{Zn^{2+}} = \frac{4}{\pi\tau}\left(\frac{mv}{MA}\right)^2\left(\frac{\Delta Es}{\Delta Et}\right)^2 \tag{4}$$

where $m$ (g) and $M$ (g mol$^{-1}$) are assigned to the loading mass and molecular weight of active material; $V$ (cm$^3$ mol$^{-1}$) represents the molar volume of materials deduced from crystallographic data; $\tau$ (s) is constant current pulse time; $A$ (cm$^2$) is the surface area of electrode; $\Delta E_s$ (V) and $\Delta E_t$ (V) denote the change of steady-state voltage and the total change of the voltage during a constant pulse for a single-step GITT curve, respectively. A current density of 200 mA g$^{-1}$ is applied to the ZIBs with $\tau$= 10 min and then stood for 60 min without current impulse.
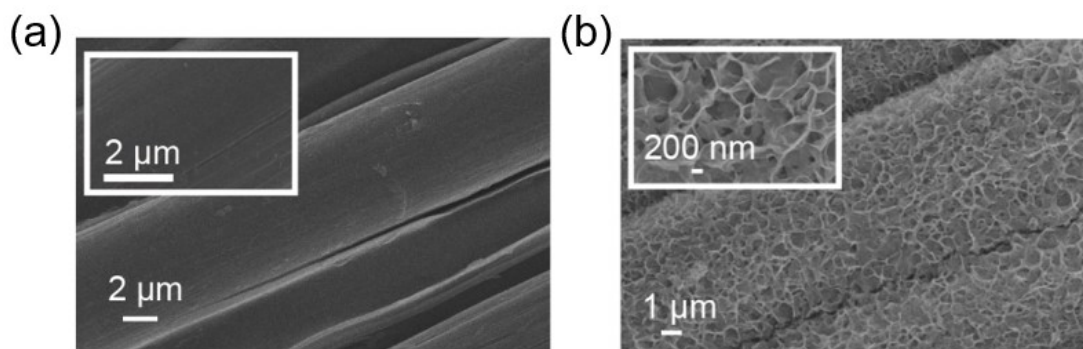
**Fig. S1.** SEM of cloth fiber and the $Mn_3Al_1$-LDH as precursor grow along the carbon fibers.
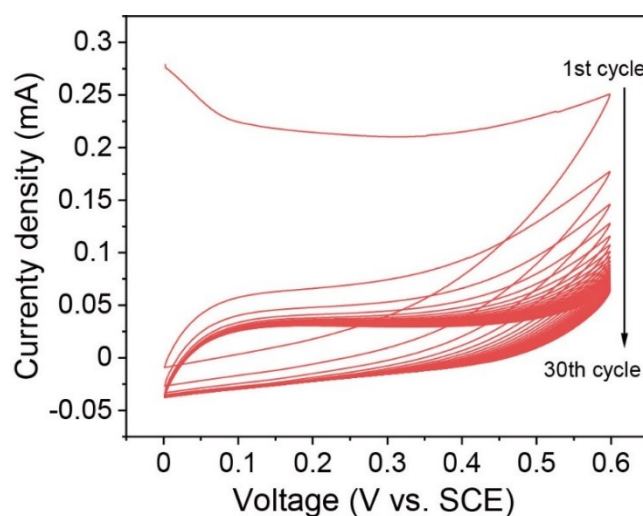


**Fig. S2. Electrochemical oxidation process of LDH phase into $MnO_2$ phase.** An electrochemical oxidation process was applied to transfer LDHs by conducting 30 cycles of cyclic voltammetry (CV) at a scan rate of 20 mV $s^{-1}$ with a potential window of 0-0.6 V *vs.* Saturated calomel electrode (SCE) in 1 M KOH electrolyte. During the electrochemical oxidation process, the LDH phase will be reconstructed into Al doping birnessite-type $MnO_2$ with Al cationic defects as described follows:

$$MnAl\text{-}LDH + x OH^- \rightarrow Al_x\text{-}MnO_2 + (1\text{-}x)Al^{3+} + x e^- + H_2O$$
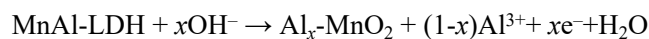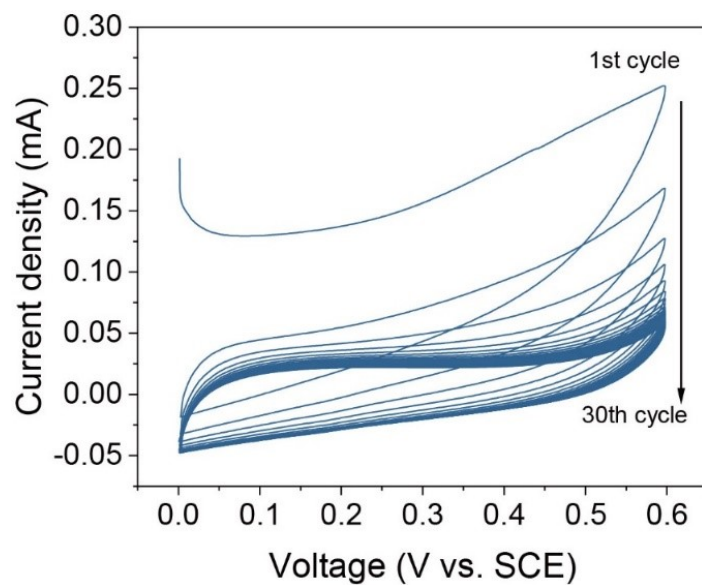
**Fig. S3**. Eelectrochemical oxidation process of $Mn(OH)_2$ into $MnO_2$.
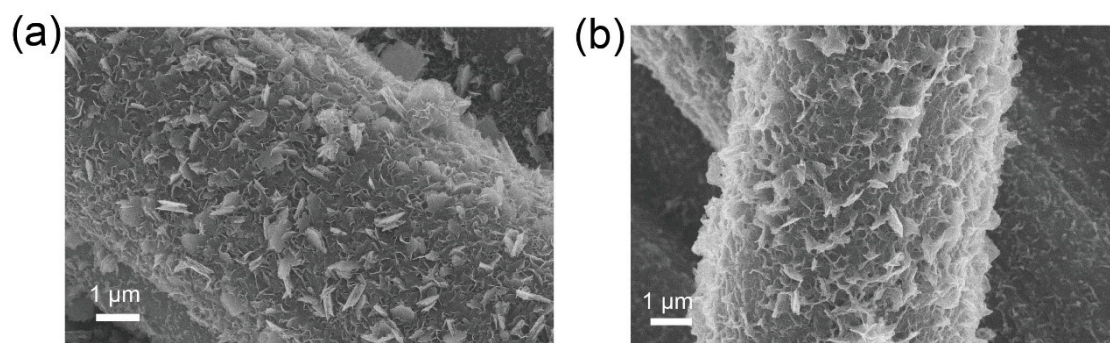


**Fig. S4.** SEM image of (a) $Mn(OH)_2$ nanosheets and (b) $MnO_2$ electrode.
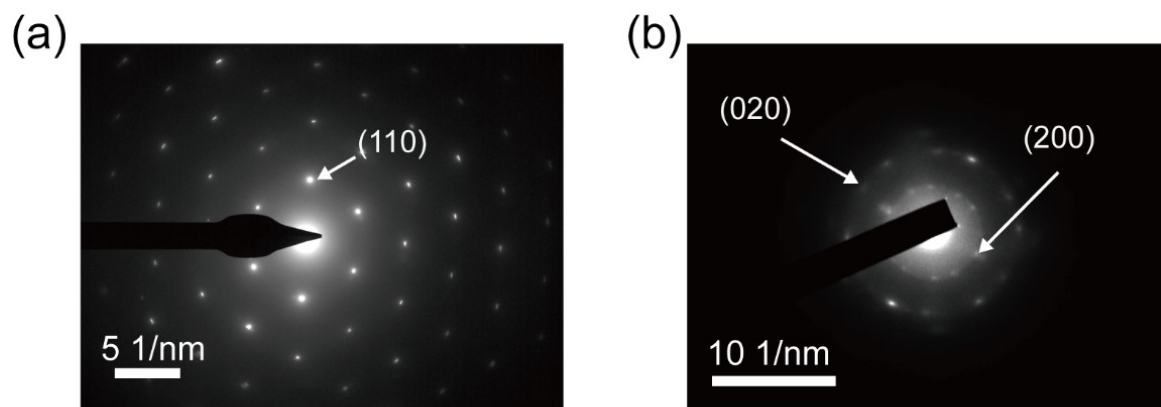
**Fig. S5.** Selected area electron diffraction (SAED) pattern of (a) $Mn_3Al_1$-LDH and (b) $Al_{0.1}$-$MnO_2$ nanosheets.
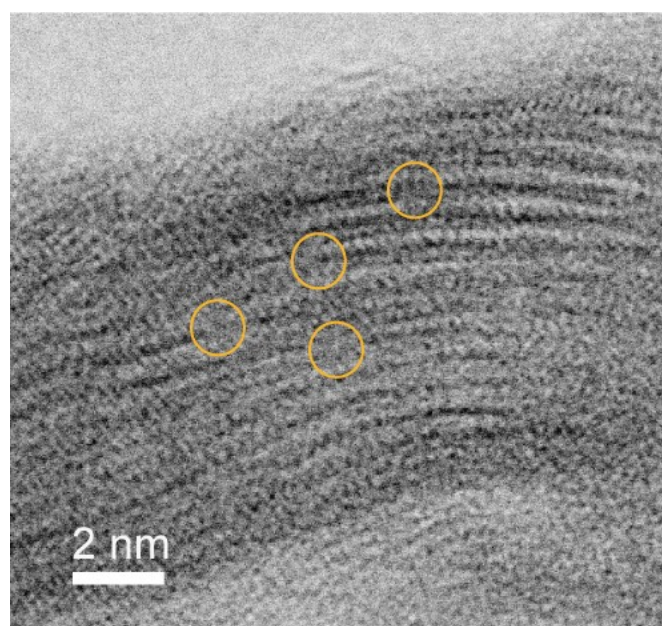


**Fig. S6**. ACTEM images of $Al_{0.1}$-$MnO_2$ along the *ab*-axis.
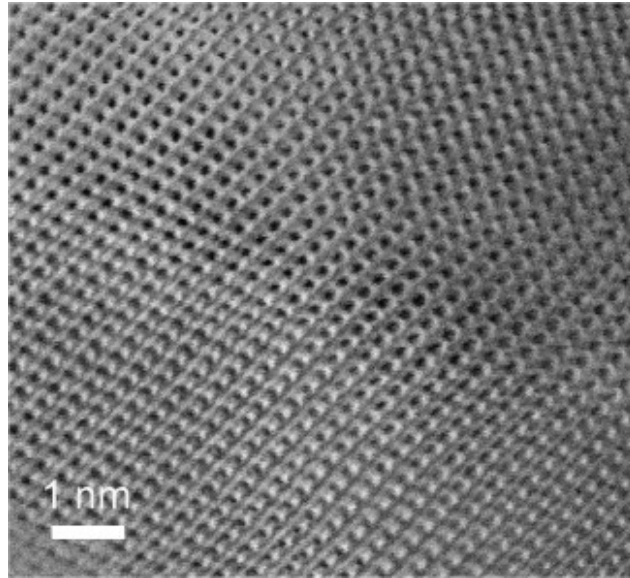
**Fig. S7.** ACTEM images of $MnO_2$.
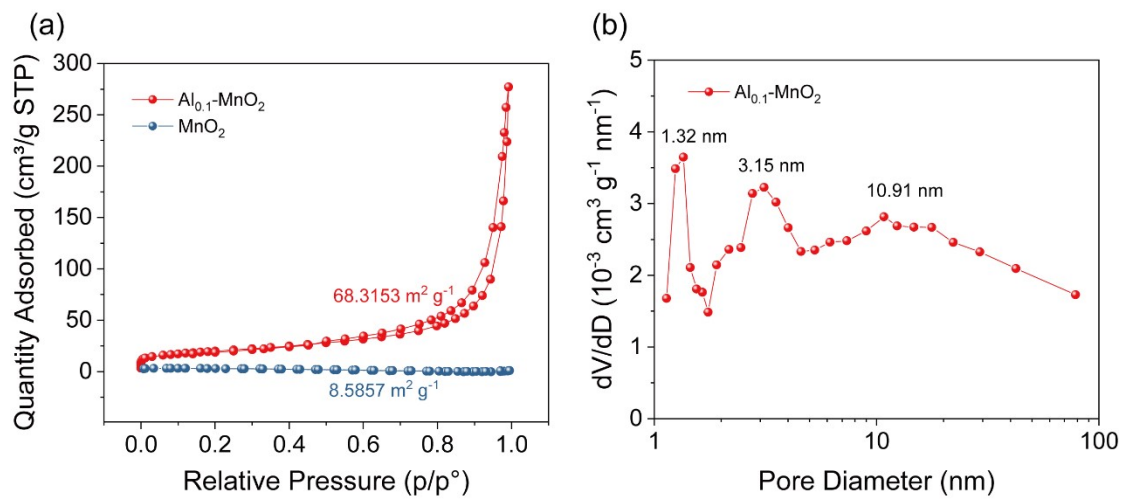


**Fig. S8.** (a) $N_2$ adsorption/desorption isotherm for $Al_{0.1}$-$MnO_2$ and $MnO_2$. (b) The corresponding pore size distribution for $Al_{0.1}$-$MnO_2$ and $MnO_2$.
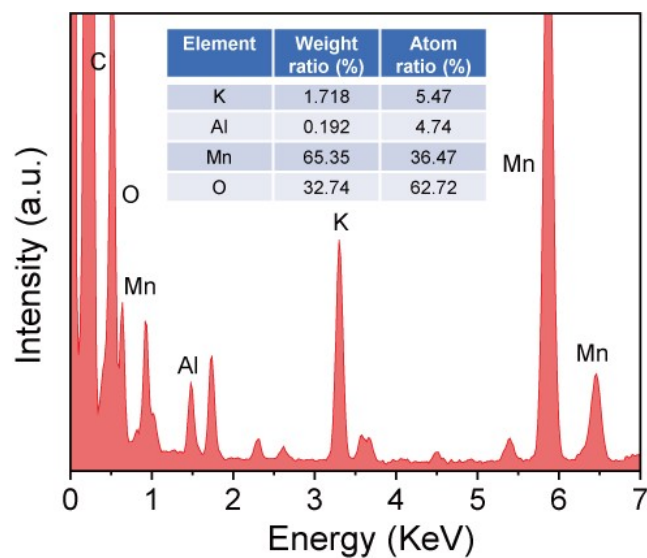
**Fig. S9.** EDS spectrum and corresponding element contents of $Al_{0.1}$-$MnO_2$.
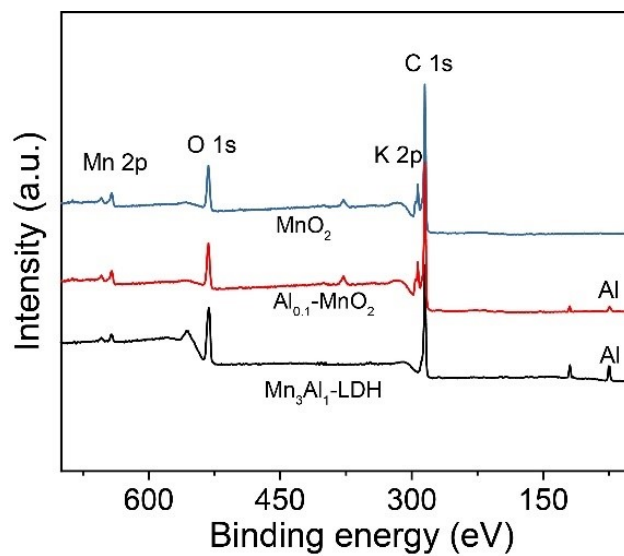


**Fig. S10.** X-ray photoelectron spectroscopy (XPS) survey spectrum of $Mn_3Al_1$-LDH, $Al_{0.1}$-$MnO_2$, $MnO_2$ electrode.
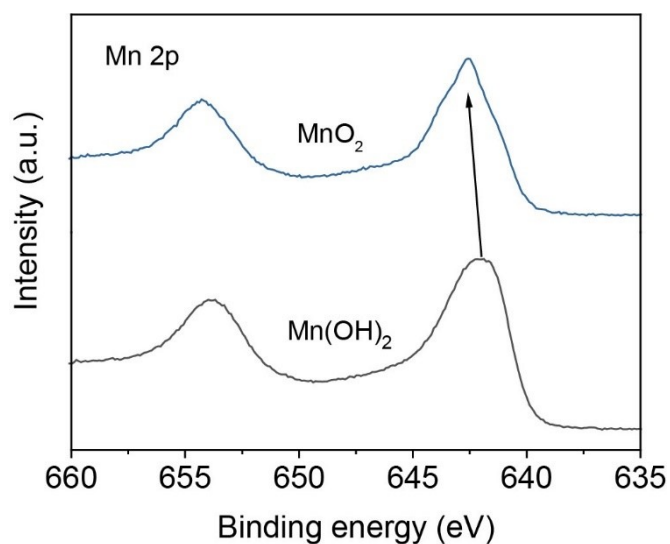
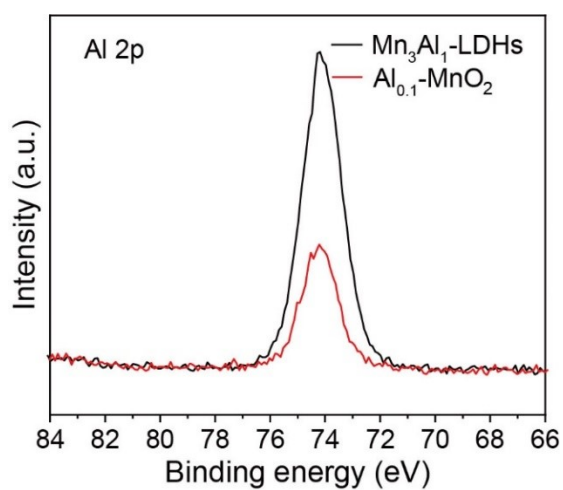**Fig. S11.** Mn 2p spectra for Mn(OH)$_2$ and MnO$_2$ electrode.



**Fig. S12.** Al 2p spectra for Mn$_3$Al$_1$-LDH and Al$_{0.1}$-MnO$_2$.
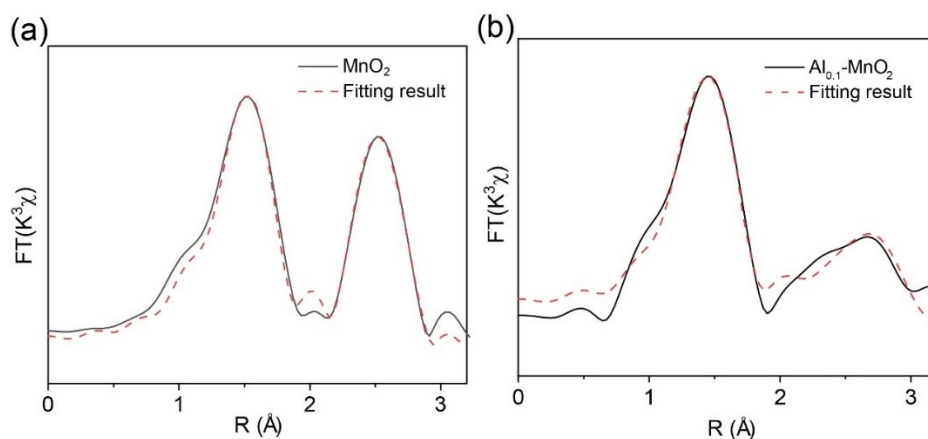
**Fig. S13.** The Fourier transformation of Mn K-edge ECAFS spectra for $MnO_2$ and $Al_{0.1}$-$MnO_2$.
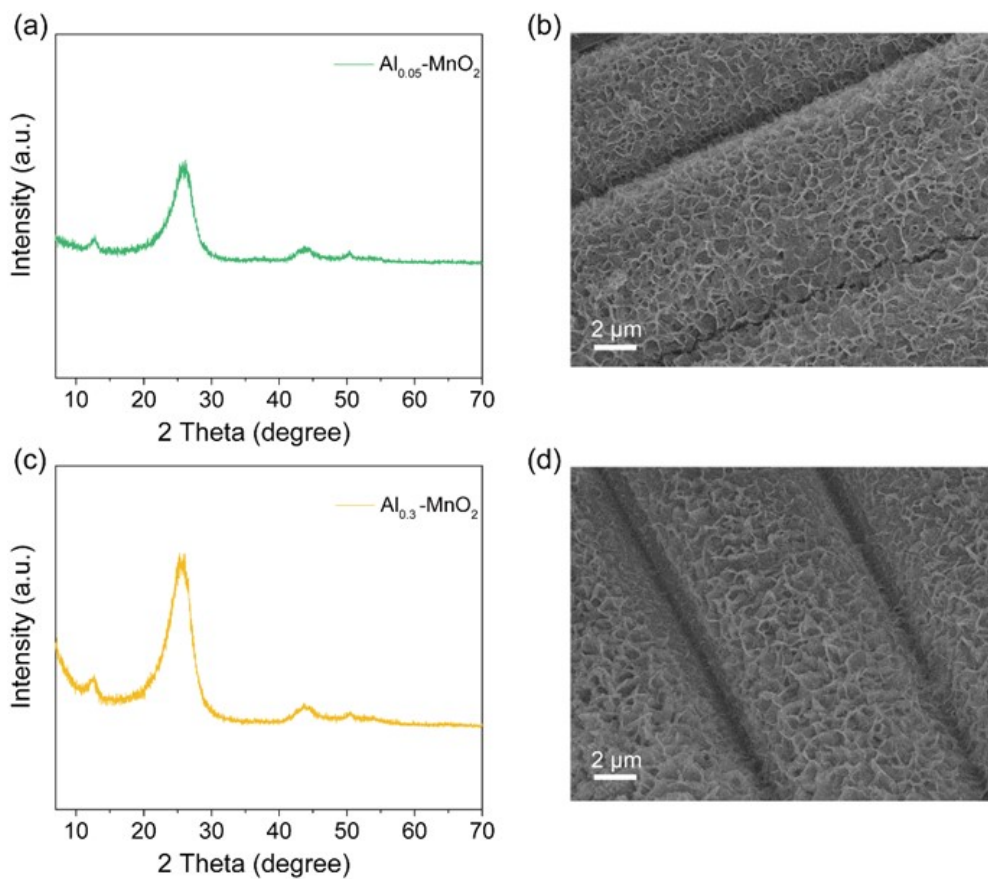


**Fig. S14.** Structural analysis of $Al_{0.05}$-$MnO_2$ and $Al_{0.3}$-$MnO_2$ cathode materials. (a) XRD pattern and (b) SEM image of $Al_{0.05}$-$MnO_2$. (c) XRD pattern and (d) SEM image of $Al_{0.3}$-$MnO_2$.
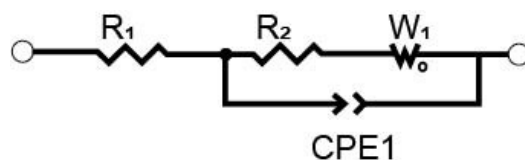
**Fig. S15.** The equivalent electrical circuit for Nyquist plots for $MnO_2$, $Al_{0.05}$-$MnO_2$, $Al_{0.1}$-$MnO_2$, and $Al_{0.3}$-$MnO_2$ electrodes.

Note to **Fig. S15**: $R_1$ is the solution resistance; $R_2$ and CPE1 are the charge-transfer impedance and the surface capacitance on the electrode, respectively; $W_0$ is a Warburg impedance related to the ion diffusion of the electrodes.[6]
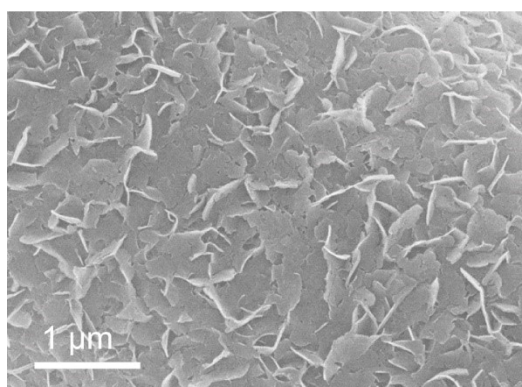


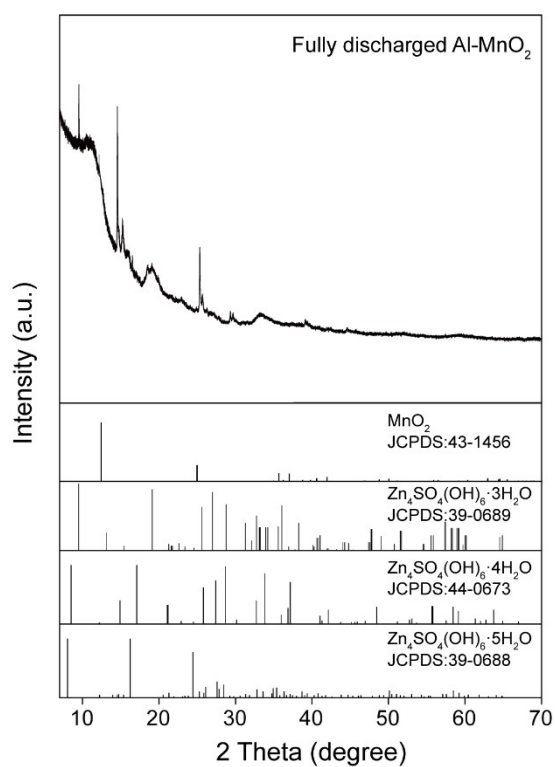**Fig. S16.** SEM image of the $Al_{0.1}$-$MnO_2$ electrode after 50 cycles at 200 mA g$^{-1}$.

**Fig. S17.** Synchrotron X-ray diffraction (SXRD) pattern of $Al_{0.1}$-$MnO_2$ cathode after fully discharged to 0.8 V.
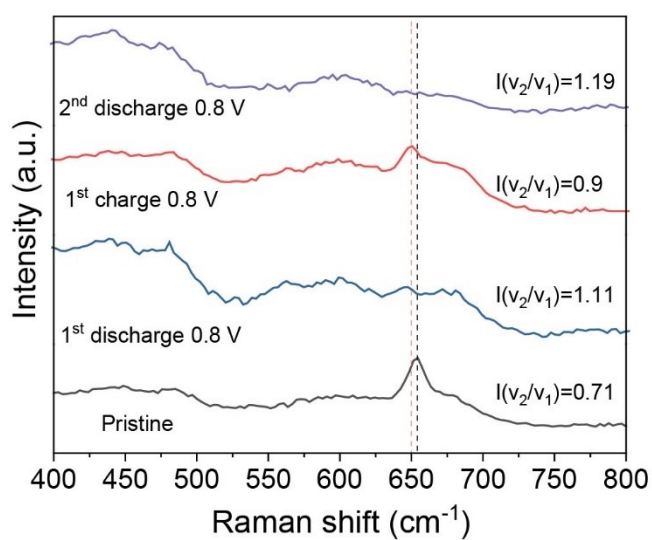


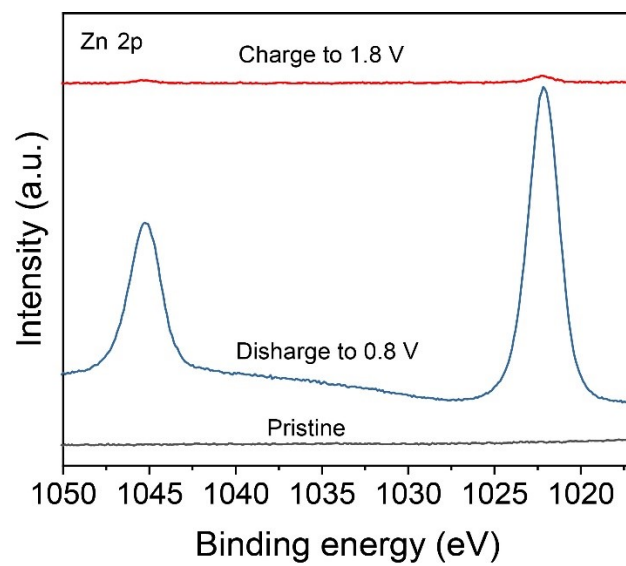**Fig. S18.** Ex-situ Raman spectra of $MnO_2$ at different voltage state.

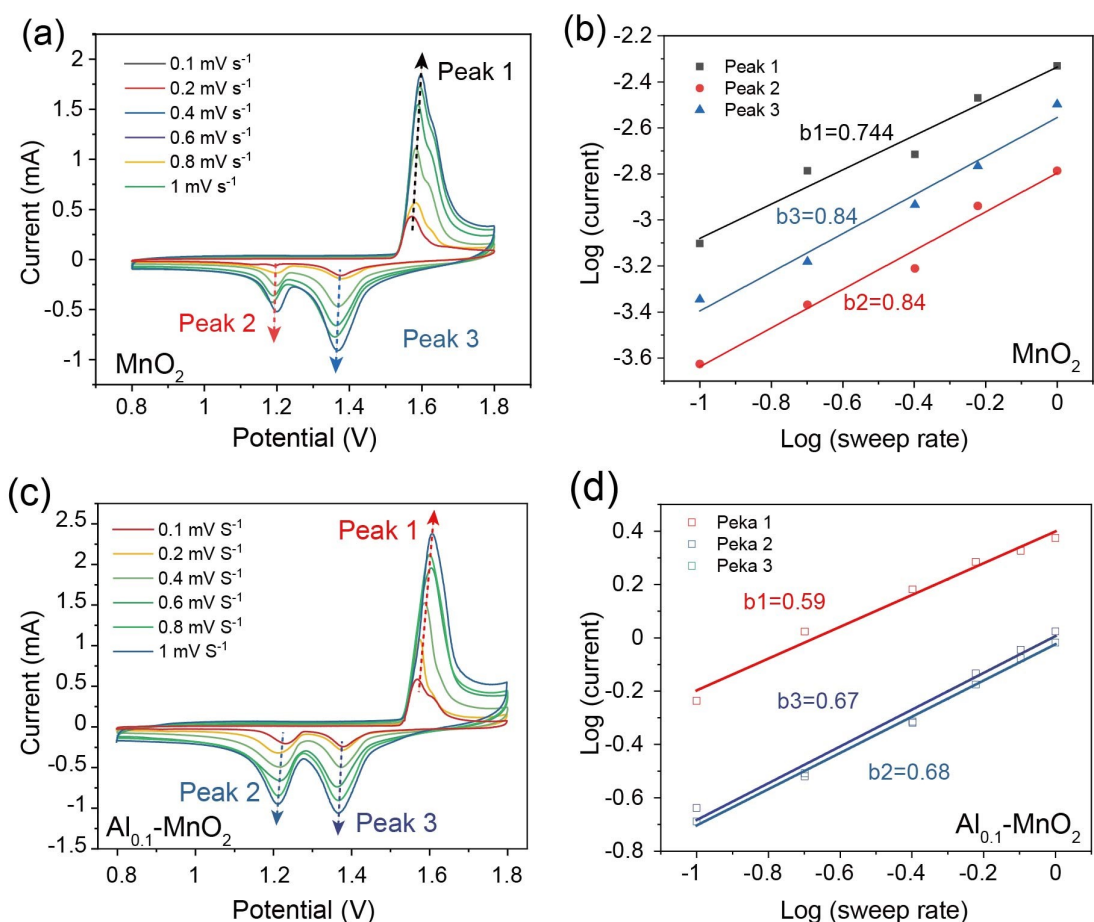**Fig. S19.** XPS spectra of Zn 2p at different voltage states in $Al_{0.1}$-$MnO_2$ electrode.

**Fig. S20.** Electrode kinetics analysis. CV curves electrode at different scan rates of (a) MnO$_2$ and (c) Al$_{0.1}$-MnO$_2$ electrode. Log (*i*) and log (*v*) plots at specific peak currents in (b) MnO$_2$ and (d) Al$_{0.1}$-MnO$_2$ electrode.

Note to **Fig. S20**: The electrochemical kinetics can be determined by the power-law function of $i_p = av^b$, where ($i_p$) is the measured peak current, a and *b* are empirical parameters, and *v* (V s$^{-1}$) is the scan rate.[5] Based on the liner fitting of log ($i_p$) versus log (*v*), the coefficient *b* values can be deduced using the slope of the linear sections. Generally, if *b* value is close to 0.5, the electrode process is mainly controlled by the diffusion process. On the other side, if *b* value is close to 1, then the surface capacitance dominates the electrochemical process[7].
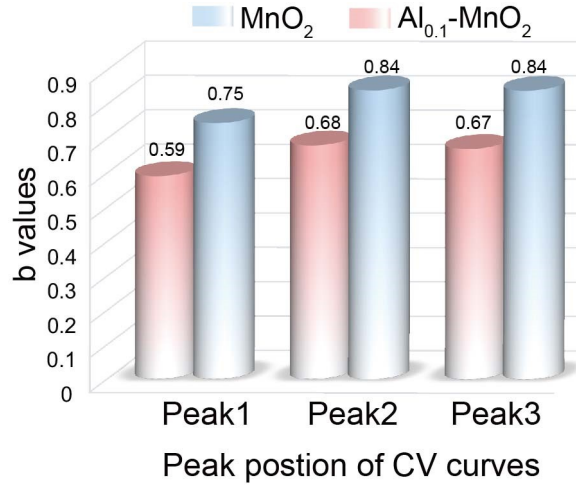
**Fig. S21.** Comparison profile of fitted $b$ values of $MnO_2$ and $Al_{0.1}$-$MnO_2$ electrode.



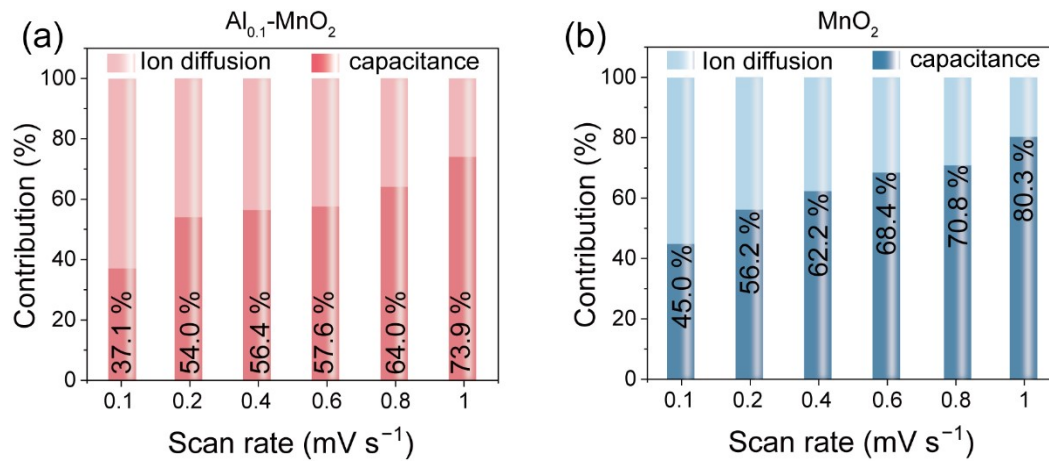**Fig. S22.** Contribution ratios of the capacitive capacities and diffusion-limited capacities at different scan rates in (a) $Al_{0.1}$-$MnO_2$ and (b) $MnO_2$ electrodes.

Note to **Fig. S22**: To distinguish the capacitive-controlled ($k_1v$) and diffusion-controlled ($k_2v^{1/2}$) contributions to the total capacity, the percentage of different contributions were quantitatively analyzed by the following equation: $i_p = k_1v + k_2v^{1/2}$, where $i_p$ was the current response at a static potential (V), $v$ was the scan rate, $k_1$ and $k_2$ were defined constants at particular sweep rates.[8]
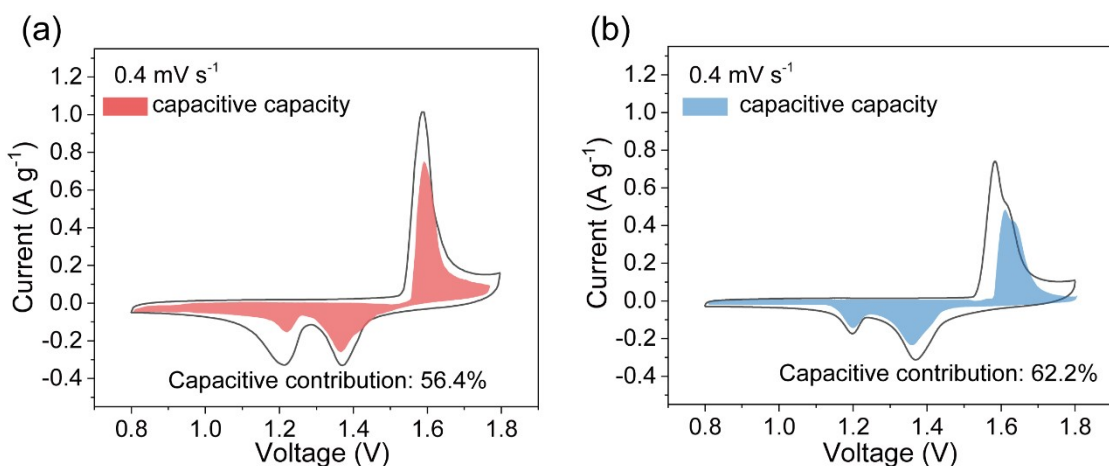
**Fig. S23.** Separation of the capacitive and diffusion-controlled current contribution at a scan rate of 0.4 mV s$^{-1}$ in (a) Al$_{0.1}$-MnO$_2$ electrode and (b) MnO$_2$ electrode.

Note to **Fig**. S23: At a scan rate of 0.4 mV s$^{-1}$, the experimentally determined specific capacities for Al$_{0.1}$-MnO$_2$ and MnO$_2$ electrodes are 321.16 and 244 mAh g$^{-1}$. Considering the theoretical capacity of 308 mAh g$^{-1}$ for MnO$_2$, the higher specific capacity of Al$_{0.1}$-MnO$_2$ electrode could be attributed to the existence of additional energy storage sites provided by structural defects. The diffusion controlled capacities of Al$_{0.1}$-MnO$_2$ (43.7%, 140.3 mAh g$^{-1}$) is higher than that of MnO$_2$ (37.8%, 92 mAh g$^{-1}$), indicating that the three-dimensional diffusion channels will facilitate Zn$^{2+}$ ions diffusion.
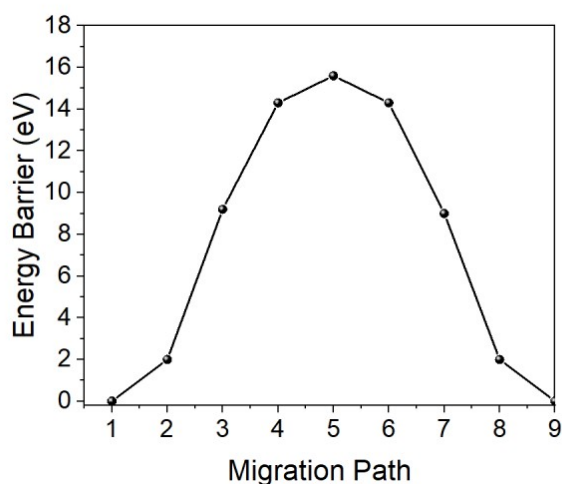


**Fig. S24.** The Zn ions across the non-defective single layer MnO$_2$ and corresponding potential energy curves.

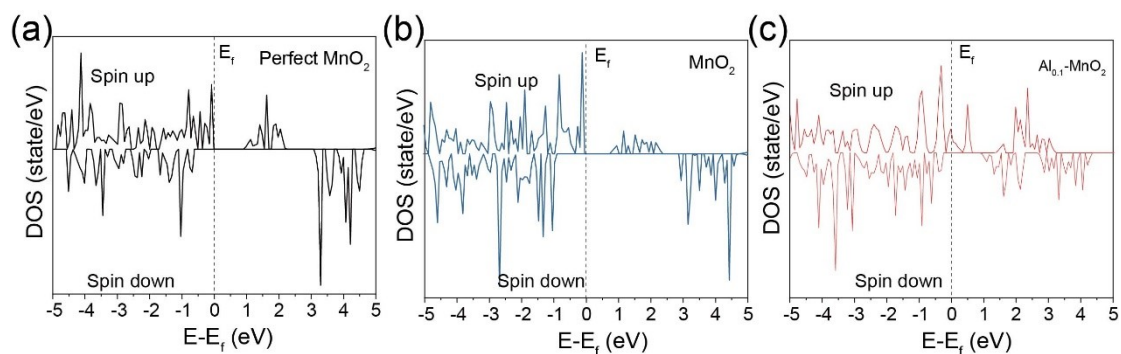**Fig. S25.** Calculated total density of states of (a) non-defective birnessite-type $MnO_2$, (b) $MnO_2$ with oxygen defects, (c) $Al_{0.1}$-$MnO_2$ with oxygen defects and cation defects.
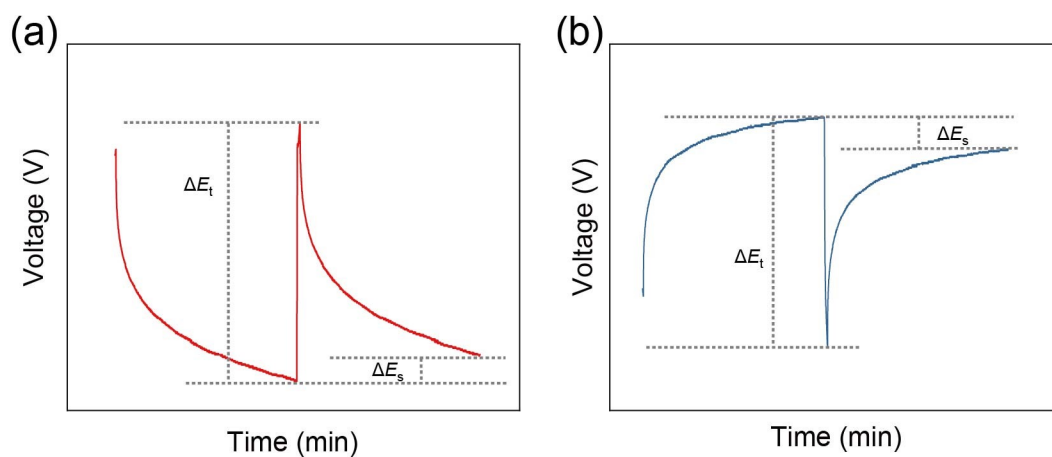


**Fig. S26.** Schematic illustration for a single step in GITT measurement: (a) Charge state (b) discharge state.
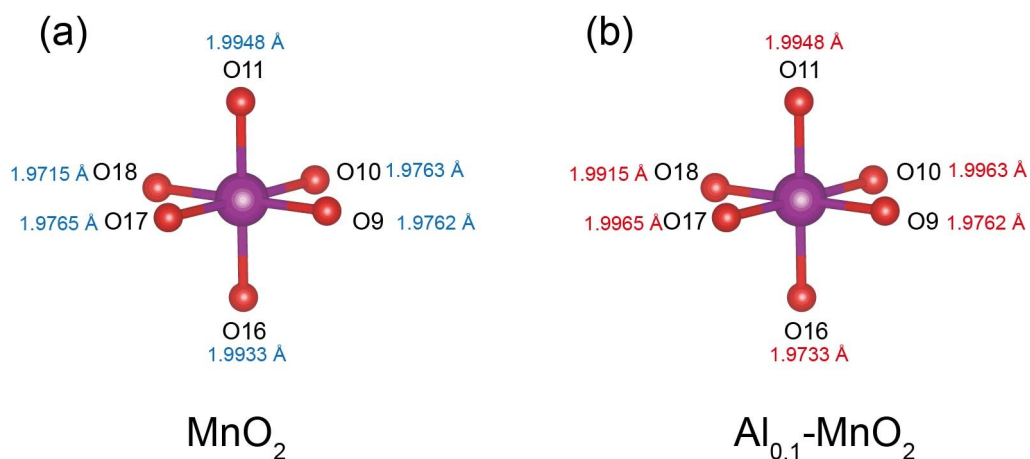
**Fig. S27.** Schematic illustration of Mn-O bonds in the Mn octahedron in $MnO_2$ and $Al_{0.1}$-$MnO_2$.



**Fig. S28.** Jahn-Teller distortion of Mn-O octahedral in $MnO_2$ and $Al_{0.1}$-$MnO_2$. The Mn-O bond length values for $MnO_2$ and $Al_{0.1}$-$MnO_2$. With valence state of $Mn^{3+}$ ion is calculated by full relaxation and energy minimization. The Mn-O distance was strongly elongated along the O11-Mn6-O16 direction, which cause serious structural distortion in $MnO_2$. In contrast, the Jahn-Teller distortion $_2$ is greatly depressed in $Al_{0.1}$-$MnO_2$.

**Table S1.** The molar ratio of Al-$MnO_2$ analysed by inductively coupled plasma spectrometry.

| Precursor | Electrode | Element | Molar ratio |
|---|---|---|---|
| $Mn_2Al_1$-LDH | Al-$MnO_2$ | K | 0.07 |
| | | Mn | 1 |
| | | Al | 0.35 |
| $Mn_3Al_1$-LDH | Al-$MnO_2$ | K | 0.15 |
| | | Mn | 1 |
| | | Al | 0.13 |
| $Mn_4Al_1$-LDH | Al-$MnO_2$ | K | 0.72 |
| | | Mn | 1 |
| | | Al | 0.05 |

**Table S2.** Local structural parameters around Mn estimated by EXAFS analysis.

| Sample | Path | $N$ | R(Å) | $\sigma^2(10^{-3}Å)$ | $\Delta E_0$(eV) | R-factor |
|---|---|---|---|---|---|---|
| $MnO_2$ | Mn-O | 5.8±1.02 | 1.8±0.04 | 4.1±0.3 | -9.5±2.0 | 0.02 |
| | Mn-Mn | 5.8±1.3 | 2.8±0.01 | 5.2±0.5 | -10.2±3.18 | |
| $Al_{0.1}$-$MnO_2$ | Mn-O | 4.4±0.6 | 1.8±0.02 | 5.1±0.5 | -8.5±1.6 | 0.02 |
| | Mn-Mn/Al | 5.4±2.8 | 2.9±0.02 | 6.9±0.7 | -8.5±1.6 | |

$N$ is the coordination number; $R$ is distance between absorber and backscatter atoms; $\sigma^2$ is Debye-Waller factor (represents the thermal and static disorder in absorber-scatterer distances); $\Delta E_0$ is the edge energy shift (the difference between the zero kinetic energy value of the sample and that of the theoretical model). $R$ factor is used to assess the goodness of the fitting.

**Table S3.** The simulated EIS parameters of $MnO_2$ and Al doped $MnO_2$.

| Samples | R1 ($\Omega$) | R2 ($\Omega$) |
|---|---|---|
| $MnO_2$ | 2.21 | 391.60 |
| $Al_{0.05}$-$MnO_2$ | 1.48 | 282.8 |
| $Al_{0.1}$-$MnO_2$ | 1.23 | 88.59 |
| $Al_{0.3}$-$MnO_2$ | 1.52 | 209.1 |

[1]     P. Hohenberg, W. Kohn, *Phys. Rev.* **1964**, *136*, B864.

[2]     W. Kohn, L. J. Sham, *Phys. Rev.* **1965**, *140*, A1133.

[3]     G. Kresse, J. Hafner, *Phys Rev B Condens Matter* **1993**, *47*, 558.

[4]     G. Henkelman, B. P. Uberuaga, H. Jónsson, *The Journal of Chemical Physics* **2000**, *113*, 9901.

[5]     X. Yang, A. L. Rogach, *Adv. Energy Mater.* **2019**, *9*, 1900747.

[6]     Y. Fu, Q. Wei, G. Zhang, X. Wang, J. Zhang, Y. Hu, D. Wang, L. Zuin, T. Zhou, Y. Wu, S. Sun, *Adv. Energy Mater.* **2018**, *8*, 1801445.

[7]     Y. Ma, M. Xu, R. Liu, H. Xiao, Y. Liu, X. Wang, Y. Huang, G. Yuan, *Energy Stor. Mater.* **2022**, *48*, 212.

[8]     J. Wang, J. G. Wang, X. Qin, Y. Wang, Z. You, H. Liu, M. Shao, *ACS Appl. Mater. Interfaces* **2020**, *12*, 34949.